Scripta Materialia 268 (2025) 116862

Contents lists available at ScienceDirect

Scripta Materialia

journal homepage: www.journals.elsevier.com/scripta-materialia

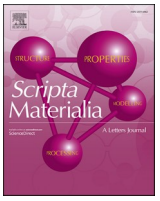

Effect of Zn and Al alloying on slip system activation and strengthening mechanisms in magnesium alloys

Gaoming Zhu [a,*], Young Min Kim [b], Ulrich Lienert [c], Dietmar Letzig [a], Sangbong Yi [d,*]

[a] Institute of Material and Process Design, Helmholtz-Zentrum Hereon, Geesthacht 21502, Germany
[b] Department of Magnesium, Korea Institute of Materials Science, Changwon 51508, Republic of Korea
[c] Deutsches Elektronen-Synchrotron (DESY), Hamburg 22607, Germany
[d] School of Materials Science and Engineering, Kumoh National Institute of Technology, Gumi 39177, Republic of Korea

ARTICLE INFO

Keywords:
Magnesium alloys
Slip system activation
Solute alloying
Three-dimensional X-ray diffraction
CRSS

ABSTRACT

The deformation mechanisms of Zn- and Al-alloyed Mg were investigated using in-situ three-dimensional synchrotron X-ray diffraction (3DXRD). The activation of basal and prismatic slip was quantified in Mg-1Al (A1), Mg-1 Zn (Z1), and Mg-1Al-1 Zn (ZA11) alloys in order to assess the influence of solute alloying on slip system competition. The results reveal that the combined addition of Zn and Al facilitates prismatic slip activation by reducing its critical resolved shear stress (CRSS), and leads to the lowest RSS_{prism}/RSS_{basal} ratio of 5.44, compared to 6.25 in A1 and 6.23 in Z1. This indicates a more balanced activation of basal and non-basal slip systems. Grain rotation analysis further suggests that ZA11 accommodates deformation more effectively through non-basal slip, reducing stress localization. These findings provide direct insights into how solute interactions influence slip system activity and offer guidelines for optimizing Mg alloys for improved ductility and mechanical performance.

Magnesium (Mg) alloys have emerged as attractive materials for lightweight structural applications due to their exceptional specific strength and low density [1–3]. However, their limited ductility and relatively low strength, governed by their hexagonal close-packed (HCP) crystal structure, hinder widespread adoption [4,5]. These inherent challenges necessitate a deeper understanding of the deformation mechanisms and strategies to improve their mechanical properties. To overcome these limitations, alloying has proven to be one of the most effective approaches for modifying deformation behavior and enhancing the strength of Mg alloys by influencing slip system activation [6,7].

Among the various alloying elements, zinc (Zn) and aluminum (Al) are two widely studied alloying elements in Mg alloys due to their significant influence on slip system activation and their ability to improve the balance between strength and ductility [8]. The addition of Zn has been shown to reduce the critical resolved shear stress (CRSS) for prismatic slip, promoting its activation and enhancing ductility [6,9,10]. Additionally, Zn solutes also influence dislocation dynamics by altering cross-slip behavior and introducing solute drag effects, which affect strain hardening and work-hardening rates [10–13]. In contrast, Al primarily contributes to solid solution strengthening by increasing the CRSS for twinning, thereby suppressing twin-mediated deformation and encouraging slip-dominated plasticity [14,15]. The synergistic addition of Zn and Al has proven highly effective in developing high-performance, rare-earth free Mg alloys, as exemplified by the widely used AZ31 series. These alloys achieve an optimal balance of strength and ductility, making them commercially viable for structural applications. However, excessive additions of Zn or Al can lead to the formation of brittle intermetallic phases or precipitate-induced stress localization, which may degrade ductility [16–18].

The combined addition of Zn and Al introduces complex solute interactions that influence deformation behavior in Mg alloys [19,20]. However, how Zn and Al interact at the grain level to modify deformation mechanisms under in-situ loading conditions has not been systematically explored. Understanding these interactions is essential for optimizing alloy design and improving the mechanical performance of Mg alloys. This study focuses on the effects of small Zn and Al additions, emphasizing their microalloying impact and interactions.

Traditional characterization techniques, such as electron backscatter diffraction (EBSD) and transmission electron microscopy (TEM), provide valuable insights into slip system activation but are limited to post-mortem analysis and surface-sensitive observations. In contrast, in-situ three-dimensional synchrotron X-ray diffraction (3DXRD) enables real-

* Corresponding authors.
E-mail addresses: gaoming.zhu@hereon.de (G. Zhu), sangbong.yi@kumoh.ac.kr (S. Yi).

https://doi.org/10.1016/j.scriptamat.2025.116862
Received 15 April 2025; Received in revised form 30 June 2025; Accepted 30 June 2025
Available online 5 July 2025

time tracking of individual grain orientations, lattice strains, and stress evolution during deformation, offering a unique capability to probe bulk deformation behavior at the grain scale [21–27]. The present study employs in-situ 3DXRD to track slip system activity in Mg-1Al (A1), Mg-1 Zn (Z1), and Mg-1Al-1 Zn (ZA11) alloys. By quantitatively analyzing the activation fractions of basal and prismatic slip, their respective resolved shear stress (RSS) ratios, and the differences in grain rotation behavior, this study provides a direct grain-level assessment into the role of Zn and Al in modulating deformation mechanisms in Mg alloys.

High-purity Mg (>99.95 %), Al (>99.99 %), and Zn (>99.99 %) were used as raw materials for preparing Mg-1.0wt %Al (A1), Mg-1.0wt %Zn (Z1), and Mg-1.0wt %Al-1.0wt %Zn (ZA11) alloys, as shown in Table 1. The raw materials were melted under a protective atmosphere of Argon at 710 °C. The melt was stirred for 30 min to ensure homogeneity before being cast into the steel molds preheated to 350 °C. The cast billets underwent homogenization at 420 °C for 16 h to eliminate segregation and promote solute uniformity. Immediately after homogenization, billets were quenched in water to retain the solution-treated state. Subsequently, the billets were hot rolled at 400 °C for 15 passes, producing final sheets with a thickness of 1.0 mm. The rolled plates were heat treated at various temperatures and times to obtain similar grain sizes among the examined alloys. The microstructures were visualized using a scanning electron microscope (SEM, Crossbeam 550 L, Zeiss, Germany) equipped with an EBSD detector (Oxford Instrument, United Kingdom). The EBSD samples were prepared by mechanical grinding followed by electro-polishing using Struers AC2.

To investigate the deformation behavior and slip system activation in Mg alloys, in-situ 3DXRD experiments were performed at beamline P21.2 of PETRA III (DESY, Hamburg, Germany). Fig. 1 illustrates the experimental setup, consisting of a high-energy monochromatic X-ray beam directed at the tensile specimen mounted within a uniaxial testing machine. The X-ray beam had an energy of 52 keV ($\lambda = 0.23843$ Å) and a size of 150 μm (height) × 2000 μm (width). A Varex XRD4343CT area detector (2880 × 2880 pixels, 150 μm pixel size) was positioned approximately 960 mm behind the sample and calibrated using a CeO_2 standard sample. The A1, Z1, and ZA11 alloys were machined into miniature tensile specimens (gauge length: 4 mm; cross-section: 1 × 1 mm^2) with the tensile axis aligned along the rolling direction (RD). These specimens were mounted on a custom-built uniaxial tensile rig equipped with a 1 kN load cell. Tensile tests were conducted at room temperature, and at a strain rate of 10^{-4} s^{-1}. 3DXRD data acquisition was synchronized with incremental tensile loading, with measurements taken up to ~2 % strain. At each loading step, the sample was rotated around its tensile axis in 0.25° increments over a range of 0° to 180°, and diffraction patterns were captured with a 0.15 s exposure per frame. The specimen deformation is recorded using two cameras, with strain field measurements derived through digital image correlation (DIC) to ensure precise strain measurement and alignment throughout the experiment (see Fig. S1). The tensile machine maintains precise alignment and rotation capabilities, as shown in Fig. 1(b). The in-situ 3DXRD data processing involved grain indexing using the FABLE software packages to extract grain level information such as orientation, lattice strain, and stress distribution. Additionally, self-developed Python scripts were utilized to calculate and analyze grain rotation, slip system activation, and the critical resolved shear stress (CRSS) of individual slip systems.

Table 1
Chemical compositions, heat treatment parameters, and average grain sizes of the A1, Z1, and ZA11 alloys.

Materials	Al (wt. %)	Zn (wt. %)	Mg (wt. %)	Heat treatment temperature (°C)	Heat treatment time (min)	Grain size (μm)
A1	1.	0	Bal.	400	15	169
Z1	0	1.	Bal.	500	30	147
ZA11	1.	1.	Bal.	400	15	158

Fig. 1(c) presents the microstructures of the A1, Z1, and ZA11 alloys, exhibiting equiaxed grains with average grain sizes of 169 μm, 147 μm, and 158 μm, respectively. The insert {0001} pole figures indicate that the three alloys exhibit similar basal textures, with basal plane normals predominantly aligned parallel to the sample normal direction (ND). The comparable texture characteristics suggest that the activation of slip systems during deformation is expected to be similar across the three alloys. The similar grain sizes and textures of these three alloys indicate that differences in their deformation behavior and mechanical properties are likely attributable to the effects of solute alloying.

The stress-strain curves of the A1, Z1, and ZA11 alloys recorded during the 3DXRD experiments are shown in Fig. 1(d). All three alloys exhibit notable differences in yield strength and ultimate tensile strength (UTS). The Z1 alloy demonstrates the highest yield strength (~76 MPa) and flow stress, indicating the significant strengthening contribution of Zn solutes. In contrast, the A1 alloy shows a lower yield strength and UTS, suggesting that Al solutes contribute less effectively to strengthening under the current experimental conditions. Notably, the ZA11 alloy, which combines Al and Zn solutes, exhibits a further reduction in strength.

The 3DXRD reconstruction identified 602 tracked grains in the A1 alloy, 407 in the Z1 alloy, and 689 in the ZA11 alloy, providing detailed grain orientation and spatial distribution information (Fig. 2). The grain orientations reconstructed by 3DXRD are in good agreement with EBSD data, particularly in capturing the basal texture (see Fig. S2). While EBSD provides high-resolution two-dimensional information on grain orientation and misorientation at the surface, 3DXRD extends this capability by enabling the analysis of bulk grain behavior within the sample. Statistical analysis of diffraction spot intensities, complemented by EBSD results, confirms that the grain size distribution obtained from 3DXRD is uniform, as shown in Fig. 2(b).

The correlation between macroscopic stress and average σ_{zz} stress for the A1, Z1, and ZA11 alloys is illustrated in Fig. 2(c). The true stress-strain curves of macroscopic stress (yellow lines) and average σ_{ZZ} stress (blue dots) exhibit strong consistency, indicating that the internal stress measured by 3DXRD closely follows the externally applied stress. At each loading step, the average σ_{zz} stress calculated from all tracked grains aligns well with the macroscopic stress, with only minor deviations attributed to heterogeneity in stress distribution among individual grains in the polycrystalline structure. A direct comparison between true stress and average σ_{zz} stress is provided in Fig. S3, further confirming the reliability of 3DXRD in capturing bulk stress states.

The grain-level σ_{zz} stress distributions during different loading steps of the A1 alloy, as shown in Fig. 3, demonstrate the progressive evolution of internal stresses under tensile loading. In the figure, symbol size is proportional to the grain size, and the color indicates the value of σ_{zz} stress. The selected loading steps correspond to 0 % strain (before deformation), 0.2 % strain (near the yield point), and 1 % and 2 % strain (in the plastic deformation regime). At the initial 0 % strain stage, most grains exhibit low stress levels, as indicated by the predominantly green color in the stress distribution map and the histogram (see Fig. S4) centered around 5 MPa. As deformation progresses, the average σ_{zz} stress increases steadily, reaching 69 MPa at 0.2 % strain, 98 MPa at 1 % strain, and 109 MPa at 2 % strain. This rise in average stress was accompanied by increasing stress heterogeneity, evident in the broader stress distribution (see Fig. S4) and the emergence of localized high-stress regions in the maps.

The bottom row of Fig. 3 illustrates the relationship between grain rotation angle and σ_{zz} stress at different loading steps. A negative correlation is observed, with slopes of −17.9 MPa/°, −8.6 MPa/°, and −6.8 MPa/° at 0.2 %, 1 %, and 2 % strain, respectively. This indicates that grains with higher σ_{zz} stress tend to exhibit smaller rotation angles, reflecting their constrained deformation behavior under tensile loading. As strain increases, these high-stress grains begin to rotate more, reducing the rotation angle gap between high- and low-stress grains.

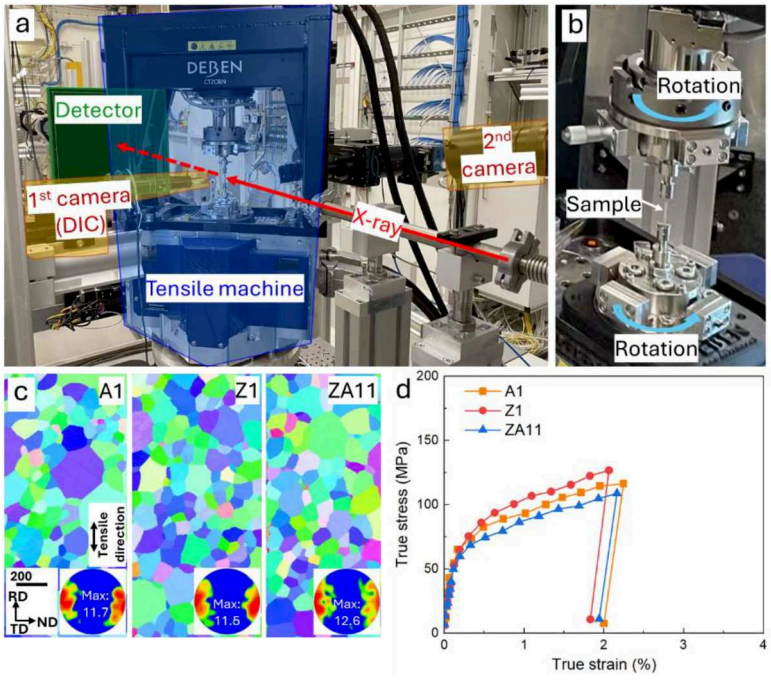

Fig. 1. (a) Experimental setup for 3DXRD, (b) a magnified view of the tensile testing machine, (c) microstructures of A1, Z1, and ZA11 alloys, and (d) true stress-strain curves recorded during 3DXRD experiments of the three alloys.

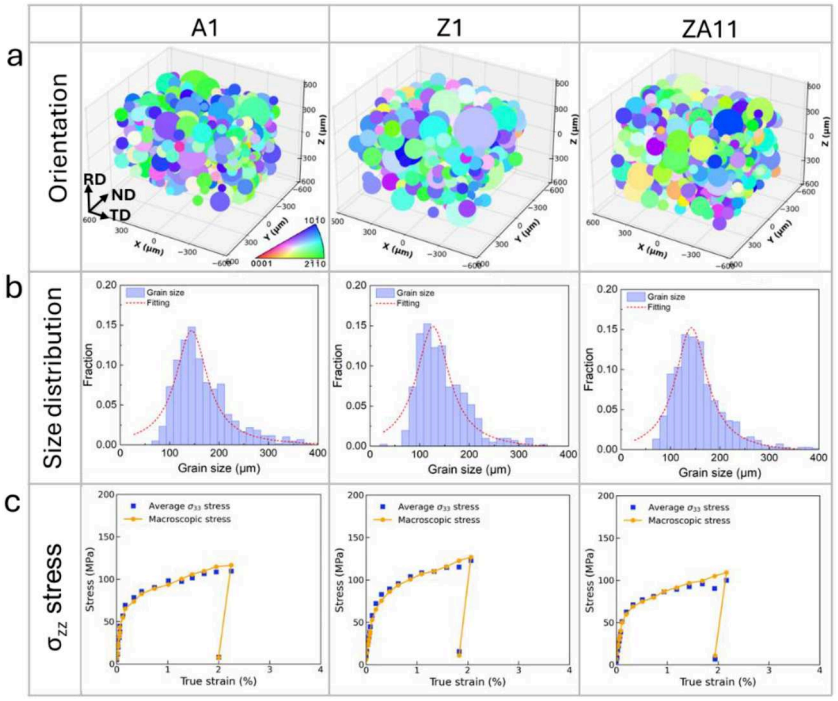

Fig. 2. (a) Grain distribution of A1, Z1, and ZA11 alloys obtained by 3DXRD reconstruction, (b) grain size distribution of the three alloys inferred from X-ray diffraction intensity, and (c) comparison of macroscopic stress and average σ_{zz} stress during tensile deformation, showing alignment between macroscopic and grain-level stresses.

Such behavior is likely attributed to the activation of non-basal slip systems, which enable grains that are otherwise resistant to rotation to accommodate strain more effectively under higher stress conditions. Statistical analysis of basal and prismatic slip grains in the A1 alloy reveals that grains with basal slip activation show higher rotation angles than those with prismatic slip activation (Fig. S5). This also explains why the slope remains negative across all strain levels.

Fig. 4(a) and (b) illustrate two grains exhibiting basal and prismatic slip, respectively. In Fig. 4(a), the c-axis tilt angle equals the rotation angle, and the rotation axis aligns with the $\langle 1120 \rangle$ direction. This suggests basal slip activation, as the CRSS for pyramidal II $\langle c + a \rangle$ slip is significantly higher and typically activates later in deformation. The inset schematically illustrates the rotation mechanism driven by basal slip. In Fig. 4(b), the c-axis tilt angle is zero, and the rotation axis aligns

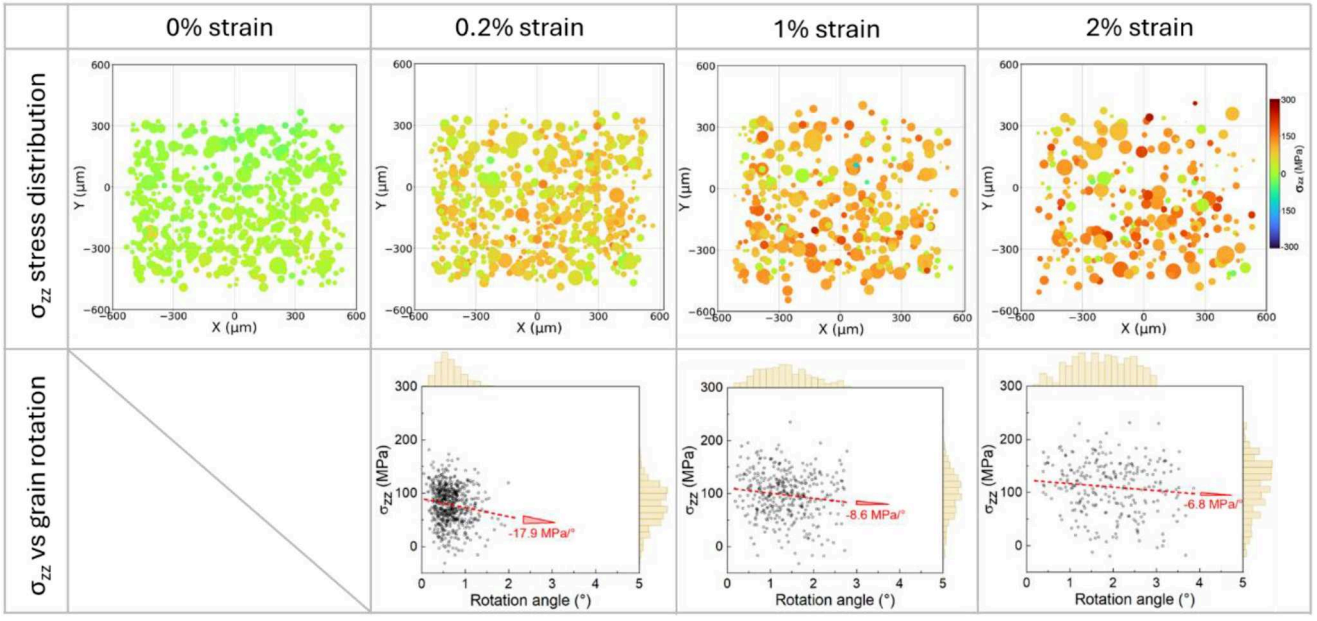

Fig. 3. Grain level σ_{zz} stress distributions and relationship between grain rotation angle and σ_{zz} stress at various loading steps (0 %, 0.2 %, 1 %, and 2 % strain) of the A1 alloy.

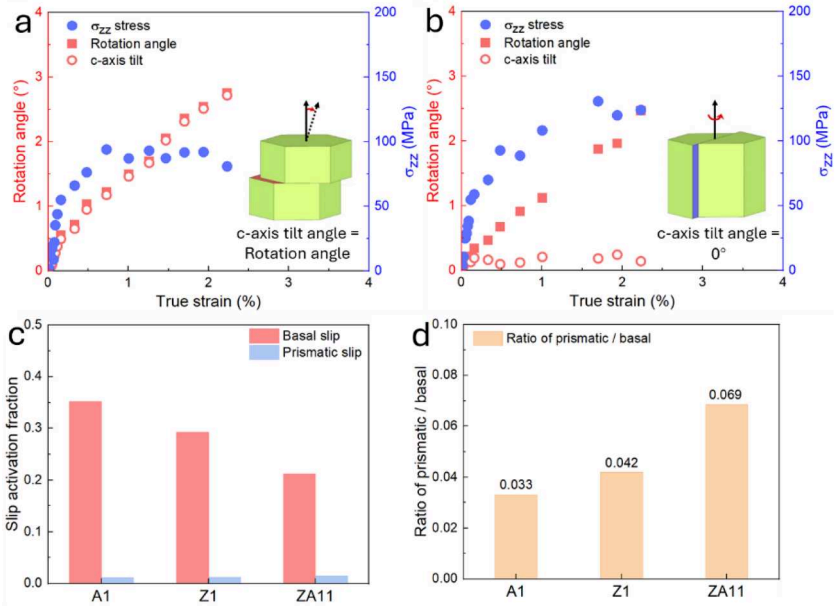

Fig. 4. Two example grains showing the activation of (a) basal slip and (b) prismatic slip, (c) activation fractions of basal and prismatic slip systems in A1, Z1, and ZA11 alloys, (d) ratio of prismatic to basal slip activation, showing the increasing importance of prismatic slip with Zn and Al alloying.

with ⟨0001⟩, indicating prismatic slip activation. The importance of prismatic slip in accommodating strain along non-basal planes and enhancing ductility was demonstrated in previous studies [28,29]. Due to 3DXRD limitations, this analysis focuses on basal and prismatic slip systems, with other non-basal mechanisms like pyramidal I ⟨a⟩ or pyramidal II $\langle c+a \rangle$ not comprehensively evaluated.

Using grain rotation analysis, the activation fractions of basal and prismatic slip systems across the three alloys were determined (Fig. 4(c)). Basal slip is dominant in all cases, while prismatic slip exhibits minimal activation in A1. The highest fraction of prismatic slip activation is observed in ZA11, suggesting a synergistic effect of Zn and Al in promoting non-basal slip. This trend is further quantified in Fig. 4(d), where the prismatic-to-basal slip activation ratio increases progressively from 0.033 in A1 and 0.042 in Z1 to 0.069 in ZA11. These results demonstrate how alloy composition influences slip system activation, affecting the overall deformation behavior.

The average grain rotation angle and c-axis tilt angle, plotted as functions of true strain in Fig. 5(a) and (b), demonstrate distinct deformation behaviors among the alloys. A1 and Z1 exhibit comparable grain rotation angles, while ZA11 consistently shows the lowest values, suggesting reduced lattice reorientation during deformation. The slightly higher rotation angle in Z1 compared to A1 indicates marginally increased dislocation activity, which may contribute to the observed higher flow stress in Fig. 1(d). The ratio of c-axis tilt to rotation angle (Fig. 5(c)) provides insights into the relative tendency for non-basal slip activation, with ZA11 exhibiting the lowest ratio across all strain levels.

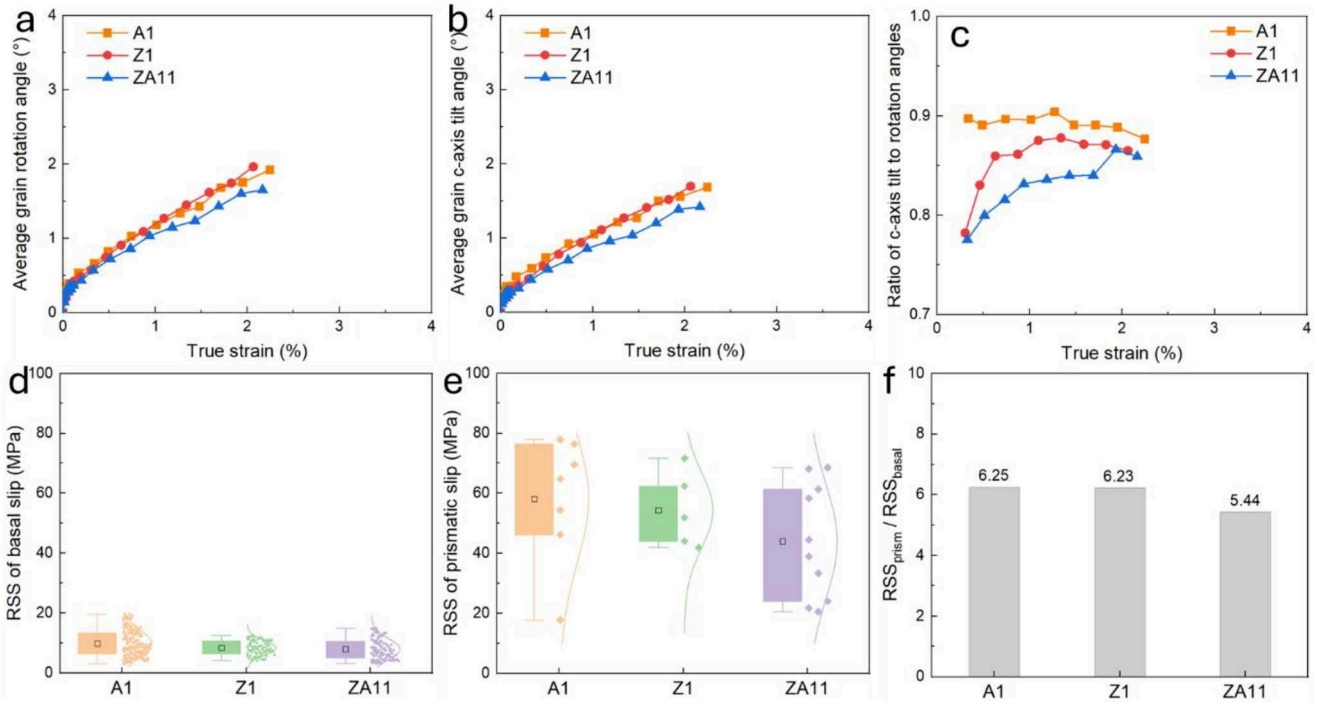

Fig. 5. (a) Average grain rotation angle and (b) c-axis tilt angle as functions of true strain of A1, Z1, and ZA11 alloys, (c) ratio of c-axis tilt to rotation angle of the three alloys, (d, e) resolved shear stresses (RSS) for basal and prismatic slips, and (f) ratios of RSS_{prism}/RSS_{basal} of the three alloys.

This trend indicates that ZA11 has the strongest propensity for non-basal slip activation, aligning with the slip system activation fractions shown in Fig. 4(c), where ZA11 displays the highest proportion of prismatic slip. These results underline the combined addition of Zn and Al in facilitating strain accommodation via non-basal slips.

The resolved shear stress (RSS) distributions of basal and prismatic slip grains, presented in Fig. 5(d) and (e), reveal the influence of alloying on slip activation at the yield point. Each dot represents an individual grain, while the box plots indicate the interquartile range (IQR), with the central square denoting the median value. The whiskers capture data variability, and the overlaid violin plots depict the probability density distribution of RSS. For both basal and prismatic slip systems, ZA11 shows the lowest RSS values, suggesting a lower resistance to slip activation compared to A1 and Z1. To further quantify this effect, the RSS_{prism}/RSS_{basal} ratio is compared across the alloys in Fig. 5(f), decreasing from 6.25 in A1 and 6.23 in Z1 to 5.44 in ZA11. This trend reinforces that ZA11 is most favorable for prismatic slip activation. A lower RSS ratio in ZA11 suggests enhanced strain accommodation through prismatic slip, potentially improving ductility and reducing anisotropy during deformation.

Based on the 3DXRD reconstructed grains in Fig. 2(a), the cumulative distribution curves of the Schmid factors for basal and prismatic slip were calculated for the three alloys (Fig. S6). The results indicate that the ability to activate slip systems is similar across all alloys, with ZA11 showing a slightly lower propensity in prismatic slip activation. However, experimental observations reveal that ZA11 activates the highest fraction of prismatic slip, suggesting that this difference in slip system activation is not texture-driven but rather influenced by the effects of solute alloying.

The activation of non-basal slips, such as prismatic slip, is a key contributor to ductility enhancement. The reduced RSS_{prism}/RSS_{basal} ratio observed in ZA11 reflects its increased tendency to activate non-basal slip systems [30], which mitigates stress concentrations and delays the onset of localized necking and failure [31]. Our 3DXRD data confirm that ZA11 exhibits the highest fraction of prismatic slip activation (Fig. 4(d)), consistent with the reduced RSS_{prism}/RSS_{basal} ratio and the enhanced strain accommodation observed in this alloy. This phenomenon plays a pivotal role in achieving an improved balance between strength and ductility in magnesium alloys. ZA11 exhibits the smallest grain rotation among the three alloys, as shown in Fig. 5(a), indicating that ZA11 grains undergo less pronounced dislocation accumulation during deformation. This reduced rotation, coupled with the lower c-axis tilt to rotation ratio in ZA11 (Fig. 5(c)), indicates its enhanced capability for non-basal slip activation, particularly prismatic slip. The activation of such mechanisms allows ZA11 to accommodate strain more efficiently.

In addition to slip, twinning may also contribute to the deformation of the alloys. However, all three alloys in this study were in the rolled condition, with a texture unfavorable for the nucleation of {1012} twin [32–34]. Moreover, the 3DXRD measurements were conducted only up to a true strain of 2 %, limiting the development of large twins. Considering these factors, twinning is expected to play a relatively minor role in the early-stage deformation of the rolling-textured alloys, compared to slip. This is consistent with our previous study on a rolled-textured Mg–3Sn–3Al alloy with an average grain size of ~100 μm, in which the twinned volume fraction was only 2.8 % even at 4 % strain [35]. For this study, we quantified the twin volume fractions in sample A1 at strain levels of 2 %, 4 %, and 8 %, which are 12.1 vol. %, 18.9 vol. %, and 32.4 vol. %, respectively (see Fig. S7). However, since the twinning shear is nearly perpendicular to the tensile axis, twinning does not contribute significantly to the macroscopic tensile strain. Instead, twinning serves to accommodate local strain heterogeneity and interacts with slip systems to coordinate the overall deformation [36]. Moreover, small twins or grains below a certain size threshold cannot be reliably tracked due to the inherent spatial resolution limitations of the 3DXRD technique. Therefore, the present study primarily focused on dislocation-based mechanisms.

From an alloy design perspective, our findings emphasize the significance of optimizing the CRSS ratios for basal and prismatic slip to achieve a favorable combination of strength and ductility [37,38]. Our previous research has shown that increasing the $CRSS_{prism}/CRSS_{basal}$ ratio can effectively enhance the ductility of magnesium alloys [39]. The results of this study demonstrate that the strategic co-addition of Zn and Al can effectively tune slip system activity, promoting prismatic slip

activation and reducing stress concentrations. This enhanced activation of non-basal slip systems not only facilitates ductility but also lowers the risk of premature failure. These findings provide a clear guideline for designing wrought magnesium alloys with improved mechanical properties for lightweight structural applications.

In summary, this study investigates deformation mechanisms in A1, Z1, and ZA11 alloys using in-situ 3DXRD. Among the three alloys, prismatic slip is most significantly activated in ZA11, reflecting enhanced non-basal slip activity with the co-addition of Zn and Al. ZA11 exhibits the lowest RSS values for both basal and prismatic slip systems, along wit h the smallest RSS_{prism}/RSS_{basal} ratio, indicating reduced slip activation barriers and a greater tendency for prismatic slip. Furthermore, ZA11 shows the smallest ratio of c-axis tilt to rotation angle, suggesting an increased capability to activate multiple non-basal slip systems. These findings highlight the synergistic effects of Zn and Al in modulating slip system activity, improving ductility, and providing valuable insights for the design of next-generation magnesium alloys with optimized strength-ductility balance.

CRediT authorship contribution statement

Gaoming Zhu: Writing – original draft, Software, Methodology, Investigation, Data curation. **Young Min Kim:** Writing – review & editing, Investigation. **Ulrich Lienert:** Writing – review & editing, Methodology. **Dietmar Letzig:** Writing – review & editing, Resources. **Sangbong Yi:** Writing – review & editing, Resources, Investigation, Funding acquisition.

Declaration of competing interests

The authors declare that they have no known competing financial interests or personal relationships that could have appeared to influence the work reported in this paper.

Acknowledgements

This work was partly financed by the National Research Foundation of Korea (NRF-2018R1A6A1A03025761). We acknowledge DESY (Hamburg, Germany), a member of the Helmholtz Association HGF, for the provision of experimental facilities. Parts of this research were carried out at the PETRA III beamline P21.2.

Supplementary materials

Supplementary material associated with this article can be found, in the online version, at doi:10.1016/j.scriptamat.2025.116862.

References

[1] B. Liu, J. Yang, X. Zhang, Q. Yang, J. Zhang, X. Li, Development and application of magnesium alloy parts for automotive OEMs: a review, J. Magnes. Alloys 11 (2023) 15–47.
[2] K. Nie, Z. Zhu, P. Munroe, K. Deng, J. Han, The effect of Zn/Ca ratio on the microstructure, texture and mechanical properties of dilute Mg–Zn–Ca–Mn alloys that exhibit superior strength, J. Mater. Sci. 55 (2020) 3588–3604.
[3] W.J. Joost, P.E. Krajewski, Towards magnesium alloys for high-volume automotive applications, Scr. Mater. 128 (2017) 107–112.
[4] T. Xu, Y. Yang, X. Peng, J. Song, F. Pan, Overview of advancement and development trend on magnesium alloy, J. Magnes. Alloys 7 (2019) 536–544.
[5] A. Vinogradov, D. Orlov, A. Danyuk, Y. Estrin, Deformation mechanisms underlying tension–compression asymmetry in magnesium alloy ZK60 revealed by acoustic emission monitoring, Mater. Sci. Eng. A 621 (2015) 243–251.
[6] D.F. Shi, A. Ma, M.T. Pérez-Prado, C.M. Cepeda-Jiménez, Activation of second-order pyramidal slip and other secondary mechanisms in solid solution Mg-Zn alloys and their effect on tensile ductility, Acta Mater 244 (2023) 118555.
[7] J. Wang, G. Zhu, L. Wang, E. Vasilev, J.-S. Park, G. Sha, X. Zeng, M. Knezevic, Origins of high ductility exhibited by an extruded magnesium alloy Mg-1.8Zn-0.2Ca: experiments and crystal plasticity modeling, J. Mater. Sci. Technol. 84 (2021) 27–42.
[8] Z.-Z. Jin, M. Zha, S.-Q. Wang, S.-C. Wang, C. Wang, H.-L. Jia, H.-Y. Wang, Alloying design and microstructural control strategies towards developing Mg alloys with enhanced ductility, J. Magnes. Alloys 10 (2022) 1191–1206.
[9] Z.H. Li, T.T. Sasaki, M.Z. Bian, T. Nakata, Y. Yoshida, N. Kawabe, S. Kamado, K. Hono, Role of Zn on the room temperature formability and strength in Mg–Al–Ca–Mn sheet alloys, J. Alloys Compd. 847 (2020) 156347.
[10] H.-S. Jang, B.-J. Lee, Effects of Zn on <c + a>slip and grain boundary segregation of Mg alloys, Scr. Mater. 160 (2019) 39–43.
[11] R. Ahmad, Z. Wu, W.A. Curtin, Analysis of double cross-slip of pyramidal I < c + a>screw dislocations and implications for ductility in Mg alloys, Acta Mater. 183 (2020) 228–241.
[12] D.F. Shi, M.T. Pérez-Prado, C.M. Cepeda-Jiménez, Effect of solutes on strength and ductility of Mg alloys, Acta Mater. 180 (2019) 218–230.
[13] D. Shi, A. Ma, M. Pérez-Prado, C. Cepeda-Jiménez, Activation of second-order <c + a>pyramidal slip and other secondary mechanisms in solid solution Mg-Zn alloys and their effect on tensile ductility, Acta Mater. 244 (2023) 118555.
[14] J.-Y. Wang, N. Li, R. Alizadeh, M.A. Monclús, Y.W. Cui, J.M. Molina-Aldareguía, J. LLorca, Effect of solute content and temperature on the deformation mechanisms and critical resolved shear stress in Mg-Al and Mg-Zn alloys, Acta Mater. 170 (2019) 155–165.
[15] J. Wang, J.M. Molina-Aldareguía, J. LLorca, Effect of Al content on the critical resolved shear stress for twin nucleation and growth in Mg alloys, Acta Mater. 188 (2020) 215–227.
[16] G. Zhu, L. Wang, J. Wang, J. Wang, J.-S. Park, X. Zeng, Highly deformable Mg–Al–Ca alloy with Al_2Ca precipitates, Acta Mater. 200 (2020) 236–245.
[17] R.E. Schäublin, M. Becker, M. Cihova, S.S.A. Gerstl, D. Deiana, C. Hébert, S. Pogatscher, P.J. Uggowitzer, J.F. Löffler, Precipitation in lean Mg–Zn–Ca alloys, Acta Mater. 239 (2022) 118223.
[18] H.-S. Jang, D. Seol, B.-J. Lee, A comparative study on grain boundary segregation and solute clustering in Mg-Al-Zn and Mg-Zn-Ca alloys, J. Alloys Compd. 894 (2022) 162539.
[19] M.Z. Bian, T.T. Sasaki, T. Nakata, Y. Yoshida, N. Kawabe, S. Kamado, K. Hono, Bake-hardenable Mg–Al–Zn–Mn–Ca sheet alloy processed by twin-roll casting, Acta Mater. 158 (2018) 278–288.
[20] R. Pei, Y. Zou, D. Wei, T. Al-Samman, Grain boundary co-segregation in magnesium alloys with multiple substitutional elements, Acta Mater. 208 (2021) 116749.
[21] H.F. Poulsen, Three-dimensional X-ray Diffraction microscopy: Mapping Polycrystals and Their Dynamics, Springer Science & Business Media, 2004.
[22] H. Abdolvand, J. Wright, A.J. Wilkinson, Strong grain neighbour effects in polycrystals, Nat. Commun. 9 (2018) 171.
[23] G. Zhu, A. Shabalin, J. Wang, U. Lienert, X. Zeng, L. Wang, Effect of strain rate on deformation mechanisms of a Mg alloy, Metall. Mater. Trans. A (2025) 1–16.
[24] F. Ashraf, R.S. Ramadhan, A. Al Mamun, J.A. Ball, E. Demir, T. Connolley, D. M. Collins, M. Mostafavi, D. Knowles, Investigating grain-resolved evolution of lattice strains during plasticity and creep using 3DXRD and crystal plasticity modelling, Acta Mater. 278 (2024) 120250.
[25] S.E. Gustafson, D.C. Pagan, P.A. Shade, M.D. Sangid, Dynamic recovery observed in distinct grains within a polycrystalline nickel-based superalloy during cyclic high temperature fatigue via high energy X-ray diffraction microscopy, Scr. Mater. 192 (2021) 37–42.
[26] Y. Hayashi, D. Setoyama, Y. Hirose, T. Yoshida, H. Kimura, Intragranular three-dimensional stress tensor fields in plastically deformed polycrystals, Science 366 (2019) 1492–1496.
[27] J.A. Ball, C. Davis, C. Slater, H. Vashishtha, M. Said, L. Hébrard, F. Steinhilber, J. P. Wright, T. Connolley, S. Michalik, others, Grain-level effects on in-situ deformation-induced phase transformations in a complex-phase steel using 3DXRD and EBSD, Acta Mater. 265 (2024) 119608.
[28] Z. Huang, L. Wang, B. Zhou, T. Fischer, S. Yi, X. Zeng, Observation of non-basal slip in Mg-Y by in situ three-dimensional X-ray diffraction, Scr. Mater. 143 (2018) 44–48.
[29] L. Wang, Z. Huang, H. Wang, A. Maldar, S. Yi, J.-S. Park, P. Kenesei, E. Lilleodden, X. Zeng, Study of slip activity in a Mg-Y alloy by in situ high energy X-ray diffraction microscopy and elastic viscoplastic self-consistent modeling, Acta Mater 155 (2018) 138–152.
[30] J. Wang, Y. Yuan, T. Chen, L. Wu, X. Chen, B. Jiang, J. Wang, F. Pan, Multi-solute solid solution behavior and its effect on the properties of magnesium alloys, J. Magnes. Alloys 10 (2022) 1786–1820.
[31] H. Abdolvand, M. Majkut, J. Oddershede, S. Schmidt, U. Lienert, B.J. Diak, P. J. Withers, M.R. Daymond, On the deformation twinning of Mg AZ31B: a three-dimensional synchrotron X-ray diffraction experiment and crystal plasticity finite element model, Int. J. Plast. 70 (2015) 77–97.
[32] M.R. Barnett, J. Wang, S.R. Kada, A. de Vaucorbeil, A. Stevenson, M. Fivel, P. A. Lynch, Grain scale bursts of plasticity in Mg-4Zn via high energy X-rays: towards twin observation in real-time, Acta Mater. 264 (2024) 119549.
[33] Y. Yue, J. Wang, J.-F. Nie, Twin-solute, twin-dislocation and twin-twin interactions in magnesium, J. Magnes. Alloys 11 (2023) 3427–3462.
[34] L. Jiang, J.J. Jonas, A.A. Luo, A.K. Sachdev, S. Godet, Twinning-induced softening in polycrystalline AM30 Mg alloy at moderate temperatures, Scr. Mater. 54 (2006) 771–775.
[35] G. Zhu, L. Wang, Y. Sun, X. Shang, J. Wang, H. Wang, X. Zeng, Grain-size effect on the deformation of Mg–3Al–3Sn alloy: experiments and elastic-viscoplastic self-consistent modeling, Int. J. Plast. 143 (2021) 103018.
[36] S. Wei, G. Zhu, C.C. Tasan, Slip-twinning interdependent activation across phase boundaries: an in-situ investigation of a Ti-Al-V-Fe (α+ β) alloy, Acta Mater. 206 (2021) 116520.

[37] A. Tehranchi, B. Yin, W. Curtin, Solute strengthening of basal slip in Mg alloys, Acta Mater. 151 (2018) 56–66.
[38] S. Zhou, T. Liu, A. Tang, Y. Huang, P. Peng, J. Zhang, N. Hort, R. Willumeit-Römer, F. Pan, Designing Mg alloys with high strength and ductility by reducing the strength difference between the basal and non-basal slips, Mater. Des. 225 (2023) 111476.
[39] G. Zhu, L. Wang, H. Zhou, J. Wang, Y. Shen, P. Tu, H. Zhu, W. Liu, P. Jin, X. Zeng, Improving ductility of a Mg alloy via non-basal slip induced by Ca addition, Int. J. Plast. 120 (2019) 164–179.